

https://doi.org/10.1070/QEL17026

Interference microscopy study of the preplasma formed on an iron target surface exposed to high-power femtosecond laser pulses

D.S. Sitnikov, A.V. Ovchinnikov, S.I. Ashitkov

Abstract. **The characteristic scale of spread of the plasma formed on the surface of a bulk iron target irradiated by a femtosecond laser pulse with an intensity of 10^{16} W cm^{-2} is measured by time-resolved interference microscopy using femtosecond pulses emitted by a Cr:forsterite laser system with an intensity contrast of 10^7. The chosen technique is demonstrated to be efficient in such measurements. It is shown experimentally that, as a result of laser pulse impact, the displacement of a plasma layer with a density exceeding critical does not exceed 30 nm.**

Keywords: *femtosecond pulse, hot electrons, electron acceleration mechanisms, interference microscopy.*

1. Introduction

The methods for simulating laser–plasma interaction processes have been constantly improving: more than ten theoretical studies on this subject area were published only in the year last (see, e.g., [1, 2]). At the same time, correct simulation of these processes calls for binding to experimental parameters, because the properties of plasma on the target surface depend on not only the target characteristics (structure, composition, thickness, and density) but also on the pulse parameters: duration, energy, power density, and polarisation. With an increase in the laser pulse intensity the pulse temporal profile becomes of prime importance. Indeed, the presence of a prepulse may lead to the formation of preplasma on the target surface, which affects the hot-electron generation efficiency. The influence of preplasma on both the processes of generation of fast electrons (their spectrum, spatial distribution, angular divergence) and their temperature was investigated in [3, 4]. Despite the fact that the objects of the aforementioned studies were pulses with intensities close to relativistic, the regularities obtained are also valid for lower intensity pulses.

In the case of an obliquely incident *p*-polarised ultrashort laser pulse ($I\lambda^2 \leqslant 10^{17}$ W cm^{-2} μm^2), hot electrons are mainly generated via two collisionless mechanisms: vacuum heating and resonance absorption (see, for example, [5]). According to the vacuum heating mechanism, which was proposed more than 30 years ago [6], electrons are pulled out from the supercritical plasma boundary by the laser pulse field into vacuum and turned backward to the target for a time equal to the electric-field oscillation half-period. The mechanism of resonance absorption of laser radiation implies that a *p*-polarised electromagnetic wave obliquely incident on inhomogeneous plasma can be absorbed with simultaneous excitation of an electron plasma wave [7]. Thereafter, it was shown by particle-in-cell (PIC) simulation [8] that the vacuum heating mechanism is dominant in the case of steep plasma density gradients L: $L/\lambda < 0.1$.

The characteristic X-rays generated in plasma by a *p*-polarised femtosecond pulse can be used as a diagnostic tool to estimate experimentally the action of a particular mechanism. To determine the dominant mechanism of hot-electron generation, experimental dependences of the K_α radiation intensity on the angle of incidence of a laser pulse on a target were obtained in [9]. The results of that study showed that the hot-electron generation in the entire angular range could occur according to both aforementioned mechanisms; the decisive factor is the characteristic size of plasma density inhomogeneity along the normal to the interface in the vicinity of critical density value. This characteristic size was not determined in [9].

In this paper we purpose a method for estimating the characteristic inhomogeneity scale using time-resolved interference microscopy (this technique was described in detail in [10, 11]), which was applied for the first time to investigate the preplasma on a target surface exposed to a femtosecond laser pulse with intensity of ~10^{16} W cm^{-2}. A distinctive feature of our study is the use of a pulsed IR laser source with an intensity contrast of 10^7.

2. Schematic of the experiment

Plasma was formed using a terawatt femtosecond IR laser system based on an active Cr:forsterite element, which generates pulses with a duration of ~80 fs, energy up to 90 mJ, and a repetition rate of 10 Hz; the pulse wavelength and bandwidth are 1240 nm and 26 nm (FWHM), respectively [12].

The dynamics of preplasma formation and expansion under the action of femtosecond pulses with an intensity of ~10^{16} W cm^{-2} was studied by time-resolved interference microscopy [13], which provides information about changes in the amplitude r_{ind} and phase Ψ_{ind} of complex reflection coefficient. This technique was previously used to investigate such processes as the formation of electron–hole plasma in semiconductors [14, 15], phase transitions in solids [11, 16], and ablation of a surface exposed to ultrashort laser pulses [17]. It was also applied to determine the optical and transport properties of plasma at an irradiation intensity of ~10^{15} W cm^{-2} [18] in order to find the strength of metals in liquid phase [19, 20]. It is based on the pump–probe scheme, in which laser radiation is divided by a beam splitter into two beams: pump (higher

D.S. Sitnikov, A.V. Ovchinnikov, S.I. Ashitkov Joint Institute for High Temperatures, Russian Academy of Sciences, ul. Izhorskaya 12, stroenie 2, 125412 Moscow, Russia; e-mail: sitnik.ds@gmail.com

Received 27 March 2019; revision received 8 October 2019
Kvantovaya Elektronika **50** (2) 179–183 (2020)
Translated by Yu.P. Sin'kov

power) and probe ones (Fig. 1). To change the laser pulse energy, a polarisation attenuator (composed of a half-wave plate and a prism polariser) was installed in each arm, and the energy was monitored using a calibrated germanium photodiode, which detected the radiation reflected from a wedge-shaped glass plate with a 5° vertex angle. The probe pulse (at the doubled frequency in a DKDP crystal, $\lambda = 620$ nm) served to illuminate the sample region under study. Our system was equipped with a Standa 8MT160-300 delay line, which allowed one to change the delay time t_{delay} between the pump and probe pulses with a step of 8 fs. Uniform illumination of the region analysed was provided by a spatial filter installed in the probe beam; it was a 1:1 Kepler telescope with a pinhole mounted in the common focal plane of the lenses.

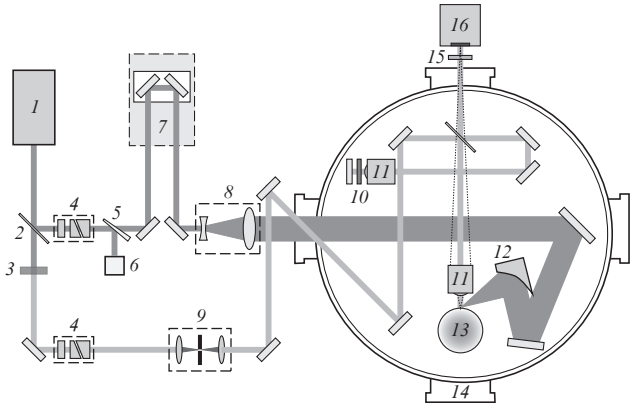

Figure 1. Schematic of time-resolved interference microscopy: (*1*) terawatt femtosecond laser system; (*2*) beam splitter; (*3*) second-harmonic generator; (*4*) polarisation attenuator; (*5*) glass wedge; (*6*) photodiode; (*7*) delay line; (*8*) telescope; (*9*) spatial filter; (*10*) set of neutral light filters; (*11*) microlens; (*12*) parabolic mirror; (*13*) sample; (*14*) vacuum chamber; (*15*) set of light filters; (*16*) CCD camera.

An interference unit (assembled according to the Michelson scheme) is mounted in the vacuum chamber. The chamber has four flanges, which make it possible to match optical windows, electrical connectors, and inlet valves. Laser radiation is introduced through the input window, which is antireflective both at the fundamental radiation wavelength of the laser system and at the second-harmonic wavelength. The chamber was evacuated to a pressure of $\sim 10^{-3}$ Torr.

The target surface image is transferred to the CCD array plane with a magnification of $M \sim 30^{\times}$ using a 9-power microlens (NA = 0.2). The second interferometer arm is formed by a microlens with similar parameters and a reference mirror. The intensities in the interferometer arms are equalised using a set of neutral light filters, installed between the reference mirror and microlens. The probe (object) beam, reflected from the sample surface, interferes with the reference beam in the plane of the CCD array, which is placed beyond the vacuum chamber. The broadband radiation of plasma was weakened by a set of light filters mounted before the array. This set included a narrowband interference light filter, transmitting at the probe pulse wavelength $\lambda_{probe} = 620 \pm 10$ nm, and light filters SZS-23, KS-11, and OS-4.

Interference patterns of the target surface were measured with a cooled SensiCam QE CCD camera (PCO CCD Imaging). They were recorded pairwise: prior to the laser impact and during it (at a certain t_{delay} value). Their processing yields a spatial distribution of the phase of complex reflection coefficient: $\Psi_{ind}(x, y)$ [13]. The error in estimating the change in the reflected wave phase, $\Delta\Psi_{ind}$, in interference microscopy is $\sim\pi/100$ [10, 11].

The target was a cylindrically shaped bulk iron sample (∅30 mm, height 35 mm) with a lateral surface roughness no worse than Rz10. To perform measurements at different points, the target was installed on a motorised target unit, consisting of Standa translation stages: three 8MT-173-20 motorised linear translation stages and one 8MR-174-11 rotational translation stage. The target was oriented so as to make the probe and the pump laser beams incident on its cylindrical surface normally and at an angle of 45°, respectively. The pump beam at the vacuum chamber input had a diameter of 35 mm and was focused by an MPD229-M01 off-axis parabolic mirror (Thorlabs) with a focal length of 50.8 mm.

3. Determination of the pump laser pulse parameters

Figure 2 shows a cross section of the third-order cross-correlation function of a high-power femtosecond laser pulse. The integral characteristics of this pulse are its temporal profile (recorded in a wide intensity range) and time contrast: the ratio of the peak power to the power of the nanosecond pedestal caused by the processes of amplified spontaneous emission (ASE) in the active elements of amplifying laser cascades. As can be seen in Fig. 2, the contrast of 1240-nm pulses is 10^7 in the range $t_{delay} = \pm 2$ ps and at nanosecond delays, whereas in the time interval $t_{delay} = \pm 1$ ps the laser pulse intensity is $\sim 10^{-4}$ of maximum, with the laser pulse duration of 100 fs (FWHM).

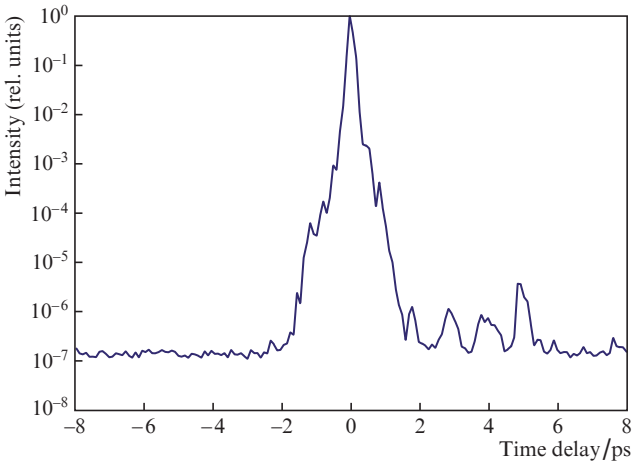

Figure 2. Cross section of the third-order cross-correlation function of a femtosecond pulse.

The spatial energy density distribution for the focused pump beam in the waist plane was estimated using the technique reported in [21], according to which the squared radius of a crater formed on the target surface as a result of its ablation is a linear function of the logarithm of laser pulse energy. To this end, the metal target was temporarily replaced with a polished single-crystal GaAs sample (craters on its surface can be distinguished well when the threshold value $F_{abl} \sim 200$ mJ cm^{-2} is exceeded). Figure 3a shows experimental dependences of the squared values of minor and major semiaxes of the ablation crater on the pump pulse energy. These dependences can

be approximated well by a set of two straight lines with different slopes. This means that the spatial intensity distribution in the focal plane of the off-axis paraboloid is described by a set of two Gaussians with widths r_{01} and r_{02} (Fig. 3b).

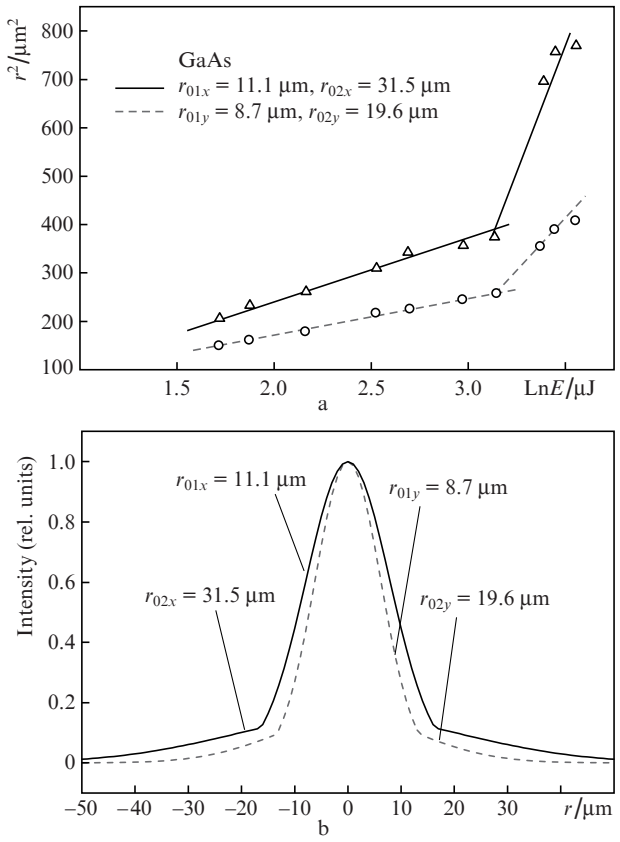

Figure 3. (a) Dependences of the squared crater radius on the pump pulse energy (GaAs target; symbols and straight lines are, respectively, experimental values and linear approximations) and (b) spatial distribution of laser beam intensity over the target surface.

This spatial distribution may be due to the laser beam wavefront aberrations caused by both the error in preparing the focusing element surface (which does not exceed, according to the manufacturer's data, $\lambda/2$ at λ = 633 nm) and the wavefront distortions in the laser source active elements. The practical consequence of this is that the central (strongly focused) part of elliptical laser spot, 24 × 32 μm in size at the level of $1/e^2$, contains 95% total pulse energy. This, in turn, means that the laser pulse energy must be 3.1 mJ to provide the laser beam intensity $I_{max} = 10^{16}$ W cm^{-2} on the target surface.

4. Experimental results and discussion

The change in the phase Ψ_{ind} of a probe reflected wave is determined by the processes occurring on the target surface and depends on the pump pulse intensity; in general, it can be written as a sum of several terms:

$$\Psi_{ind} = \Psi_{oc} + \Psi_{shift} + \Psi_{pl}, \quad (1)$$

where Ψ_{oc} is the accumulated phase difference due to the change in the optical constants of material as a result of its melting; Ψ_{shift} is the accumulated phase difference caused by the expansion of target material and the shift of plasma layer with a density on the order of critical, from which the probe pulse is reflected; and Ψ_{pl} is the phase change due to the probe pulse propagation through the plasma layer of subcritical density. The phase difference Ψ_{oc} may have different signs: it is negative in semiconductors (e. g., in Si and GaAs), whereas in metals it may be either larger (Au) or smaller (W) than zero. Figure 4a presents as an example the spatial distributions of reflected probe pulse phase Ψ_{ind}, which have been obtained previously in interference microscopy experiments at a fivefold excess of silicon and gold ablation thresholds and delays of 200 fs and 5 ps. The experiments performed in [22] showed that, at a delay time of 200 fs, one can derive information about the optical constants of a target from the data on the change in the amplitude and phase of its complex reflection coefficient only at pump pulse intensities lower than 2×10^{13} W cm^{-2}. At higher intensities the accumulated phase differences caused by the motion of the layer with critical density exceed the phase differences caused by a change in the optical constants of target material: $\Psi_{shift} \gg \Psi_{oc}$. The accu-

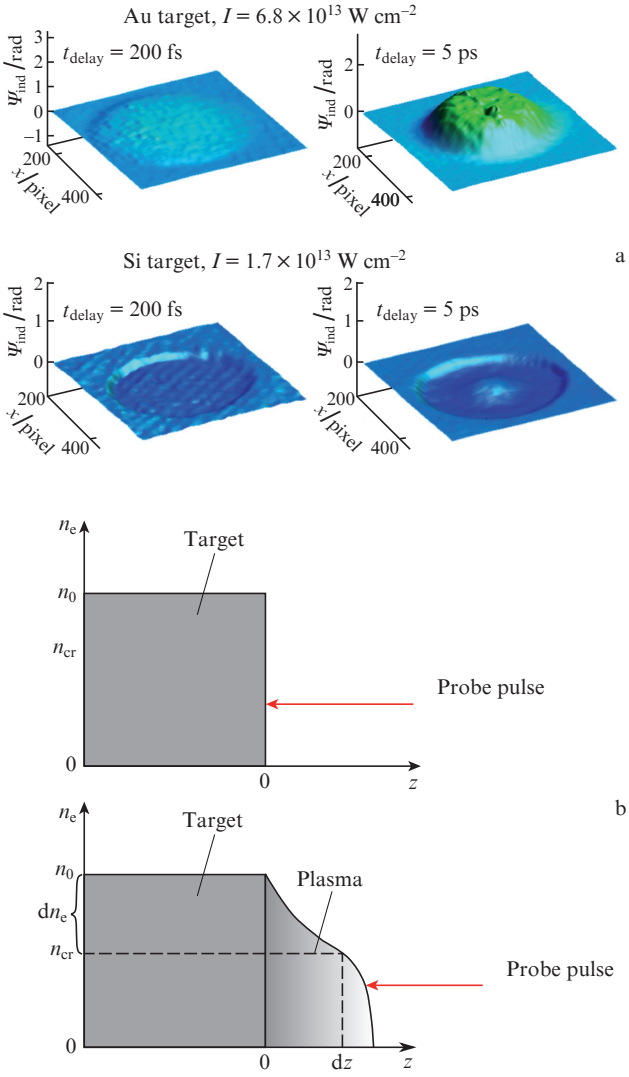

Figure 4. (a) Change in the phase of a probe reflected wave under the action of femtosecond laser pulse on metals and semiconductors (experimental data) and (b) the schematic of probe pulse reflection from target surface before (top) and after (bottom) the pump pulse action.

mulated phase difference Ψ_{oc}, which is due to the change in the optical constants during laser irradiation of a Fe target, is positive: $\Psi_{oc} > 0$ [23]. As can be seen in Fig. 4a, the experimental scheme provides also a positive value of phase difference Ψ_{shift}. Taking into account the conclusions of [22] for gold and the fact that the pump pulse intensity used by us, $I_{max} = 10^{16}$ W cm^{-2}, exceeds the value reported in [23] by three orders of magnitude, one can suggest that $\Psi_{oc} \ll \Psi_{shift}$.

To reveal the physical meaning of the term Ψ_{pl} , we demonstrate two cases of probe pulse reflection in Fig. 4b: prior to the pump pulse action (top) and during the expansion of the plasma formed on the target surface as a result of laser irradiation (bottom). In the former case the electron density profile has a stepwise shape, which corresponds to the target–vacuum interface. In the second case the probe radiation, being reflected off from the layer with critical density, propagates through the plasma layer accumulating a positive phase difference: $\Psi_{pl} > 0$. Thus, all three terms in (1) are positive.

As was shown by us previously in [9], when determining the mechanism of fast-electron generation, a key issue is the spatial scale of hydrodynamic preplasma expansion by the instant at which the pump pulse intensity is maximum. Preplasma can be formed as a result of ionisation of the vapour cloud formed by the target evaporation under nanosecond ASE at the laser pulse front edge. To study the effect of the nanosecond ASE pedestal on the target surface, the changes in the phase Ψ_{ind} were also measured at negative delays t_{delay}. The zero instant ($t_{delay} = 0$) in this experiment was taken to be the time moment at which the maxima of intensity profiles of the pump and probe pulses coincide. At a time delay $t_{delay} = -2$ ps the pump pulse intensity on the target surface is $\sim 10^{-7} I_{max}$, a value lower than the ablation threshold for the target material.

Figure 5a presents the temporal profile of the pump laser pulse intensity in the time interval $t_{delay} \pm 3$ ps. The dependence of the phse change on the complex reflection coefficient on the time delay in the range of -1.7 ps $< t_{delay} < 1$ ps is plotted in Fig. 5b. These experimental data show that the accumulated phase difference Ψ_{ind} is $\sim 0.58 \pm 0.12$ rad at zero delay ($t_{delay} = 0$). The error in determining this value is conditioned by not only the accuracy of the technique used to process Fourier interference patterns but also by the error in determining the zero delay, $\Delta t_{delay} \pm 60$ fs, which is conditioned by the laser pulse duration.

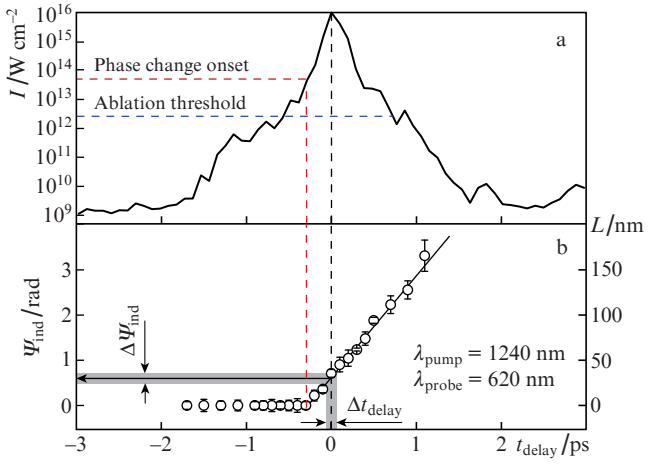

Figure 5. (a) Laser pulse temporal profile and (b) the dynamics of change in the phase Ψ_{ind} of plasma complex reflection coefficient (on the left) and the characteristic scale of plasma density inhomogeneity L (on the right).

Taking into account the above assumptions, the experimental estimate of the accumulated field difference Ψ_{ind} can be written as the sum of two terms:

$$\Psi_{ind} = \Psi_{shift} + \Psi_{pl} = 0.58 \pm 0.12 \text{ rad}. \quad (2)$$

Since each of the aforementioned values is nonnegative, one can state that the change in the phase Ψ_{shift} caused by the preplasma spread is below 0.58 rad. The shift of the plasma layer with the critical density $n_{cr} = 2.9 \times 10^{21}$ cm^{-3} (for probe radiation with a wavelength $\lambda = 620$ nm) does not exceed $dz = \Psi_{shift}\lambda_{probe}/4\pi < 29$ nm in this case, and the velocity of the critical-density layer is $\sim 10^5$ m s^{-1}. Note that the character of the plasma expansion (in particular, the sign of Ψ_{shift}) may be fairly sensitive to the prepulse shape. The case of 'good' contrast, where the ablation threshold is obtained for less than 1 ps before the main pulse arrival, was considered above. Under conditions of poor contrast, when the ablation threshold is obtained much earlier, the situation with the motion of a critical-plasma layer appears to be not so unambiguous.

The estimated characteristic scale of plasma spread, $L = [(1/n_e)(dn_e/dz)]^{-1}$ [6], corresponding to the change in the complex reflection coefficient phase, is also shown in Fig. 5b. The dn_e value was taken to be the difference between the initial and critical densities (for the probe wavelength $\lambda = 620$ nm): $dn_e = n_0 - n_{cr}$ (see Fig. 4b). The estimated shift of the critical-density layer was used as the dz value. This approach makes it possible to evaluate the plasma inhomogeneity scale only in the linear approximation, i.e., on the assumption that the electron density changes linearly with an increase in the distance from the target surface. Thus, the estimates based on the aforementioned assumptions showed that plasma with a characteristic inhomogeneity size $L < 30$ nm was formed on the target surface at the instant corresponding to maximum laser pulse intensity.

As was noted in [9], the optimal conditions for forming electrons with energies ~ 10 keV to generate characteristic radiation (provided by the vacuum heating mechanism) are observed when the plasma inhomogeneity size L is small in comparison with the electron oscillation amplitude in the electric field of the laser radiation component oriented normally to the target surface. According to [8], the criterion here is the validity of the condition $L/\lambda < 0.1$, which corresponds to the characteristic scale of plasma inhomogeneity $L \sim 120$ nm for an IR laser pulse.

5. Conclusions

The formation and expansion of plasma as a result of the processing of a bulk iron target by pulsed radiation from a femtosecond Cr:forsterite laser system at a wavelength of 1240 nm and pulse intensity $I_{max} = 10^{16}$ W cm^{-2} with a time contrast of 10^7 were experimentally investigated. Time-resolved interference microscopy was applied for the first time to estimate the characteristic scale of preplasma inhomogeneity. On the assumption that the recorded changes in the phase of the probe wave reflected from the preplasma layer with critical density are determined mainly by the plasma expansion, the characteristic scale of inhomogeneity L at the instant when the laser pulse intensity becomes maximum was found to be less than 30 nm. The results obtained indicate that vacuum

heating may be the dominant mechanism of electron acceleration under our experimental conditions.

Acknowledgements. All experiments were performed using the unique scientific facility 'Terawatt Femtosecond Laser Complex' at the Centre of Collective Use 'Femtosecond Laser Complex' of the Joint Institute for High Temperatures of the Russian Academy of Sciences.

The work was supported by the Presidium of the Russian Academy of Sciences ('Condensed Matter and Plasma at High Energy Densities' Programme I. 13).

References

1. Cantono G., Sgattoni A., Fedeli L., Garzella D., Réau F., Riconda C., Macchi A., Ceccotti T. *Phys. Plasmas*, **25**, 031907 (2018).
2. Svedung Wettervik B., Gonoskov A., Marklund M. *Phys. Plasmas*, **25**, 013107 (2018).
3. Yang X.H., Ma Y.Y., Xu H., Shao F.Q., Yu M.Y., Yin Y., Zhuo H.B., Borghesi M. *Laser Part. Beams*, **31**, 379 (2013).
4. Lin X.X., Li Y.T., Liu B.C., Liu F., Du F., Wang S.J., Chen L.M., Zhang L., Liu X., Liu X.L., Wang Z.H., Ma J.L., Lu X., Dong Q.L., Wang W.M., Sheng Z.M., Wei Z.Y., Zhang J. *Laser Part. Beams*, **30**, 39 (2012).
5. Gibbon P., Förster E. *Plasma Phys. Control. Fusion,* **38**, 769 (1996).
6. Brunel F. *Phys. Rev. Lett.*, **59**, 52 (1987).
7. Freidberg J.P., Mitchell R.W., Morse R.L., Rudsinski L.I. *Phys. Rev. Lett.*, **28**, 795 (1972).
8. Gibbon P., Bell A.R. *Phys. Rev. Lett.*, **68**, 1535 (1992).
9. Agranat M.B., Andreev N.E., Ashitkov S.I., Ovchinnikov A.V., Sitnikov D.S., Fortov V.E., Shevel'ko A.P. *Pis'ma Zh. Eksp. Teor. Fiz.*, **83**, 80 (2006).
10. Temnov V.V., Sokolowski-Tinten K., Zhou P., von der Linde D. *Appl. Phys. A Mater. Sci. Process.*, **78**, 483 (2004).
11. Temnov V.V., Sokolowski-Tinten K., Zhou P., von der Linde D. *J. Opt. Soc. Am. B*, **23**, 1954 (2006).
12. Agranat M.B., Ashitkov S.I., Ivanov A.A., Konyashchenko A.V., Ovchinnikov A.V., Fortov V.E. *Quantum Electron.*, **34**, 506 (2004) [*Kvantovaya Elektron.*, **34**, 506 (2004)].
13. Sitnikov D.S., Komarov P.S., Ovchinnikov A.V., Ashitkov S. *Zh. Tekh. Fiz.*, **79**, 75 (2009).
14. Temnov V.V., Sokolowski-Tinten K., Zhou P., El-Khamhawy A., Von Der Linde D. *Proc. Conf. Lasers Electro-Optics, 2007 (CLEO 2007)*, **237403**, 1 (2007).
15. Agranat M.B., Ashitkov S.I., Anisimov S.I., Ovchinnikov A.V., Shvartsburg A.B., Sitnikov D.S., Fortov V.E. *Appl. Phys. a-Mater. Sci. Process*, (2009).
16. Inogamov N.A., Zhakhovskii V.V., Ashitkov S.I., Khokhlov V.A., Petrov Y.V., Komarov P.S., Agranat M.B., Anisimov S.I., Nishihara K. *Appl. Surf. Sci.*, **255**, 9712 (2009).
17. Ashitkov S.I., Komarov P.S., Ovchinnikov A.V., Struleva E.V., Zhakhovskii V.V., Inogamov N.A., Agranat M.B. *Quantum Electron.*, **44**, 535 (2014) [*Kvantovaya Elektron.*, **44**, 535 (2014)].
18. Komarov P.S., Ashitkov S.I., Ovchinnikov A.V., Sitnikov D.S., Veysman M.E., Levashov P.R., Povarnitsyn M.E., Agranat M.B., Andreev N.E., Khishchenko K.V., Fortov V.E. *J. Phys. A Math. Theor.*, **42**, 214057 (2009).
19. Ashitkov S.I., Inogamov N.A., Komarov P.S., Zhakhovsky V.V., Oleynik I.I., Agranat M.B., Kanel G.I., Fortov V.E. *AIP Conf. Proc.*, **1464**, 120 (2012).
20. Ashitkov S.I., Komarov P.S., Ovchinnikov A.V., Struleva E.V., Agranat M.B. *JETP Lett.*, **103**, 544 (2016) [*Pis'ma Zh. Eksp. Teor. Fiz.*, **103**, 611 (2016)].
21. Liu J.M. *Opt. Lett.*, **7**, 196 (1982).
22. Morikami H., Yoneda H., Ueda K., More R.M. *Phys. Rev. E*, **70**, 035401 (2004).
23. Struleva E.V., Ashitkov S.I., Komarov P.S., Khishchenko K.V., Agranat M.B. *J. Phys. Conf. Ser.*, **774**, 012098 (2016).